Full paper

Stable high-voltage aqueous pseudocapacitive energy storage device with slow self-discharge

Hemesh Avireddy[a], Bryan W. Byles[c,d], David Pinto[c,d], Jose Miguel Delgado Galindo[a], Jordi Jacas Biendicho[a], Xuehang Wang[c,d], Cristina Flox[a], Olivier Crosnier[e,f], Thierry Brousse[e,f], Ekaterina Pomerantseva[c,d], Joan Ramon Morante[a,b], Yury Gogotsi[c,d,*]

[a] IREC, Catalonia Institute for Energy Research, Jardins de les Dones de Negre 1, 08930, Sant Adrià de Besòs, Spain
[b] Faculty of Physics, University of Barcelona, Barcelona, Spain
[c] Department of Materials Science & Engineering, Drexel University, Philadelphia, PA, 19104, USA
[d] A.J. Drexel Nanomaterials Institute, Drexel University, Philadelphia, PA, 19104, USA
[e] Institut des Matériaux Jean Rouxel (IMN), CNRS UMR 6502-Université de Nantes, 2 rue de la Houssinière BP32229, 44322, Nantes Cedex 3, France
[f] Réseau sur le Stockage Electrochimique de l'Energie, FR CNRS 3459, 80039, Amiens Cedex, France

ARTICLE INFO

ABSTRACT

We demonstrate an asymmetric supercapacitor in a potassium acetate-based water-in-salt electrolyte, where 2-D titanium carbide MXene and manganese oxide were used as negative and positive electrode materials, respectively. Use of water-in-salt electrolyte enables the assembled asymmetric device to be operated up to a cell voltage of 2.2 V, which overcomes the limited cell voltage issue in aqueous pseudocapacitors (1.2 - 1.4 V). This cell shows excellent rate capability (~48%) between 5 and 100 mV s⁻¹ and good stability (~93%) throughout 10,000 charge-discharge cycles (at 1 A g⁻¹) and 25 h voltage-hold at 2.2 V, which is competitive when compared with the performance of known asymmetric supercapacitors designed with activated carbon electrodes and fluorinated-imide based water-in-salt electrolytes. Moreover, our device shows slower self-discharge and ~32% higher volumetric energy density than activated carbon-based supercapacitors and is promising for applications where volumetric energy density is critical.

1. Introduction

Pseudocapacitive materials store electric charge by fast redox reactions [1,2]. Cyclic voltammetry profiles of this charge storage mechanism are similar to those of double-layer capacitors [1,3–5]. Furthermore, as most pseudocapacitive materials have high specific weight, the electrode made of these materials often display packing densities greater than 1 g cm⁻³. Both factors, contributes to a higher volumetric capacitance (> 50 F cm⁻³ [6,7]) than porous carbon-based electrodes (15–25 F cm⁻³ [2,8]). Therefore, pseudocapacitive materials are more promising than porous carbons, specifically in applications where the size or volume of the device is critical [8]. RuO_2 [9,10], IrO_2 [11], $H_{3+x}IrO_4$ [12], MnO_2 polymorphs [13], V_2O_5 [14], Fe_3O_4 [15], $FeWO_4$ [16], $Ba_{0.5}Sr_{0.5}Co_{0.8}Fe_{0.2}O_{3-\delta}$ [17], $MnFe_2O_4$ [18], $ZnMn_2O_4$ [19], $La_{1-x}Sr_xMnO_3$ [11] are examples of oxides which store charge via pseudocapacitive behavior. Most of these oxides exhibit superior capacitance values in aqueous electrolytes, but since the electrochemical potential of water-splitting reaction is low in aqueous electrolytes,

supercapacitors fabricated with these materials operate within a restricted voltage window (less than 1.23 V) [20]. The narrow cell voltage results in a limited energy density for devices operated in aqueous-based electrolytes since the energy in a supercapacitor is proportional to the square of the cell voltage, as shown by Eq. (1):

$$E = \frac{CV^2}{2}, \tag{1}$$

where E is the energy (J), C is the capacitance (F) and V is the cell voltage (V).

The use of super-concentrated solutions, such as water-in-salt electrolytes, is a promising approach to increase cell voltage and thus address the issue of limited energy densities of aqueous-based capacitors. In water-in-salt electrolytes, the amount of salt is greater than water (mass_salt/mass_water or volume_salt/volume_water > 1) [21,22], which reduces the kinetics of water splitting reactions and allows for widening of the cell voltage window [22]. For instance, the use of 21 m (mol kg⁻¹) lithium bis(trifluoromethane)-sulfonimide (LiTFSI) enables the

extension of the electrochemical potential window of MnO_2 up to 1.4 V, which was previously limited to 1.0 V in standard aqueous electrolytes [23]. However, the fade of capacitance with the increase of scan rate was higher in 21 m LiTFSI ($< 20\%$) compared to standard aqueous electrolytes ($> 45\%$, 5 M $LiNO_3$) [23]. For MnO_2 electrode, such a fast decay was attributed to lower ionic conductivity of 21 m LiTFSI ($< 10\,mS\,cm^{-1}$) over standard aqueous electrolytes ($> 50\,mS\,cm^{-1}$) [23], which was related to the strong electrostatic interaction between cation's and anion's in 21 m LiTFSI. Recently, it was found that due to the weak Lewis acidity of potassium ions, or weak interaction of acetate anion's [24,25], potassium acetate-based water-in-salt electrolytes exhibits higher ionic conductivities ($> 20\,mS\,cm^{-1}$) than LiTFSI based water-in-salt electrolytes ($< 10\,mS\,cm^{-1}$) [24,26]. Also, an electrolyte concentration of 21 m potassium acetate represents a reduction of water molecules in the solvation shell of potassium ions, as demonstrated previously by Tian et al. by Raman characterization [27]. Therefore, the use of 21 m potassium acetate as a water-in-salt electrolyte appears to enhance the rate capability of asymmetric pseudocapacitors.

Beyond using a concentrated electrolyte, the use of suitable electrode material is required for achieving high rate capability in supercapacitors. So far, only MnO_2 has been reported to show pseudocapacitance in water-in-salt electrolytes [23,28]. The properties of charge storage in MnO_2 vary significantly between polymorphs as well as with the type of electrolyte used [29]. There are many polymorphs of MnO_2 whose crystal structures differ in the arrangement of MnO_6 octahedra, including tunnel and layered crystal structures [13,26]. Birnessite, Spinel, Ramsdellite, Todorokite, Cryptomelane, Pyrolusite and OMS-5 are some known polymorphs of MnO_2. Among these, Cryptomelane (α-MnO_2) can show high rates, as it exhibits a higher electronic conductivity ($9\,mS\,cm^{-1}$) than other polymorphs ($< 3\,mS\,cm^{-1}$ [13,26]). However, due to the formation of soluble species (Mn^{2+}) within the negative potentials (*vs.* Ag/AgCl) [29], MnO_2 is limited to the positive potential windows. Therefore, it is important to find a material which shows pseudocapacitive behavior under negative potentials, which would allow designing an asymmetric supercapacitor with an expanded voltage window [30–34]. Considering this, a 2-D MXene such as titanium carbide (Ti_3C_2) is a promising electrode material to pair with MnO_2, as it demonstrates high electronic conductivity ($> 5,000\,S\,cm^{-1}$) and exhibits high volumetric capacitance in a negative electrochemical windows *vs.* Ag/AgCl ($\sim 1500\,F\,cm^{-3}$) [35–37]. According to Shpigel et al. [38] and Sugahara et al. [39], the capacitive-like charge storage is due to the intercalation of hydrated cation ions within the interlayer spacing of Ti_3C_2 MXene, and Kim et al. [40] has reported that the use of highly concentrated electrolytes such as hydrate melt of Li $(TFSI)_{0.7}(BETI)_{0.3}.2H_2O$ allows the dense accumulation of hydrated cations in the MXene interlayers enhancing the values of capacitance.

Taking account of these properties, the use of Ti_3C_2 MXene as a negative electrode coupled with a positive MnO_2 electrode in a concentrated potassium acetate-based water-in-salt electrolyte can enable an asymmetric supercapacitor. Given this motivation, herein we demonstrate a 2.2 V high-voltage asymmetric supercapacitor in a 21 m of potassium acetate-based water-in-salt electrolyte, where Ti_3C_2 MXene and α-MnO_2 are implemented as negative and positive electrodes, respectively. We discuss the electrochemical performance of this device in terms of rate capability, long-term cycling stability and self-discharge and compare its cycling stability with the recently reported hybrid cell using water-in-salt electrolytes.

2. Materials and methods

2.1. Synthesis of α-MnO₂

α-MnO_2 nanowires were prepared as previously described [40]. 316 mg of potassium permanganate ($KMnO_4$, 99 + %, Acros Organics) and 108 mg of ammonium chloride (NH_4Cl, 99.5%, Strem Chemicals) were dissolved in 100 mL of deionized water, and 20 mL of this solution

was added to a 23 mL Teflon-lined stainless steel autoclave (Parr Instrument Company). The autoclave was placed in an oven at 150 °C for 48 h, after which the product (α-MnO_2) was filtered, washed, and dried at 100 °C for 12 h.

2.2. Synthesis of Ti₃C₂ MXene

2-D Ti_3C_2 MXene was synthesized using a minimally intensive layer delamination method (MILD) [37]. 1 g of MAX phase powder of titanium aluminum carbide MAX (Ti_3AlC_2, Carbon Ukraine, particle size $< 40\,\mu m$) was added slowly to a mixture of 1 g of lithium fluoride (LiF, 98.5% grade, Alfa Aesar) in 20 ml of 9 M hydrochloric acid (HCl, 37 wt%, Alfa Aesar) to chemically etch the aluminum from the MAX phase. The reaction was stirred with a Teflon-bar for 24 h at 35 °C. The products were transferred to a 50 mL centrifugation tube and washed with deionized water by centrifugation at 3500 rpm (5 min per cycle) until the pH of the dark-green supernatant was > 5.5. The change in color indicates the beginning of delamination. After gathering the supernatant, settled and swollen sediment at the bottom of the centrifuge tube was collected and dispersed in deionized water (by shaking). Resulting black slurry was vacuum-filtered on a Celgard membrane 3501 (Celgard®) to form free-standing films which were dried in a vacuum oven at 120 °C overnight and then stored in a vacuum desiccator for further use.

2.3. Microstructural characterization

The morphology of MnO_2 and Ti_3C_2 films were characterized by scanning electron microscopy (SEM) using a Zeiss Supra 50VP (Germany) equipped with an Oxford Instruments energy dispersive X-ray spectroscopy (EDS). X-ray diffraction (XRD) was carried out on a Rigaku Smartlab (Tokyo, Japan, 40 kV, and 30 mA) and a Rigaku MiniFlex (Tokyo, Japan, 40 kV and 15 mA) diffractometer using Cu Kα.

2.4. Electrolyte preparation and measurements of the conductivity

Stoichiometric amount of anhydrous potassium acetate salt (CH_3COOK, 99 + %, Sigma-Aldrich) and of lithium bis (Trifluoromethane)-Sulfonimide (LiTFSI, 99 + %, Sigma Aldrich) were dissolved in Ar-bubbled deionized water via magnetic stirring until a homogeneous solution was obtained. Prior to the electrochemical studies, the electrolyte solution was deaerated by Ar purging. The ionic conductivity of electrolyte solutions was measured using the potentiostatic mode of electrochemical impedance spectroscopy (PEIS) at 22 °C using a two-electrode Swagelok cell. The Swagelok cell consists of a polytetrafluoroethylene body and two stainless pistons (grade 304). The measurements were done using a VMP-3 potentiostat-galvanostat (Bio-Logic, France). Frequencies applied for the measurements were taken from 1 MHz to 50 mHz, whereas an amplitude of $\pm$ 10 mV was used as applied potential. The ionic conductivity, κ (mS cm^{-1}), is calculated as:

$$\kappa = \left(\frac{1}{R_i}\right).\ k_c,$$

(2)

where, k_C is the constant, whose value is between 0.95 (max.) to 0.73 (min.). An aqueous 0.1 M KCl solution was used as a standard. The ionic resistance, R_i (mΩ cm) is taken from the intercept of the real part of impedance in the Nyquist plot. Ionic conductivity was also measured for 21 m of Lithium bis(Trifluoromethane)-Sulfonimide and later compared with values of 21 m potassium acetate solution. The resistivity of Ti_3C_2 MXene and α-MnO_2 was evaluated by four-point measurements using a probe station (ResTest v1, Jandel Engineering Ltd., Bedfordshire, U.K.). Resistivity values were averaged with 3 measurements.

2.5. Electrochemical characterization

Measurements were carried out using a VMP-3 potentiostat/galvanostat (Bio-Logic, France), in a T-shape Swagelok cell. The cell body was made up of polytetrafluoroethylene. Polished glassy carbon was used as the current collector(s) (CHI Instruments). This cell body was used as a three-electrode configuration. Capacitance, C (F) is calculated as:

$$C = \frac{1}{v. \, V} \int_{V_-}^{V_+} I(V)dV,$$ (3)

where, V (V) is the potential and v (mV s^{-1}), the scan rate. V_+ and V_- is the value of vertex potential in the positive and negative electrochemical window. I (mA) is the current response to the applied voltage, in the cyclic voltammetry technique. The capacity (mAh) is calculated as:

$$Capacity = \frac{C. \, V}{3.6}$$ (4)

Specific capacitance (F g^{-1} or F cm^{-3}) or capacity (mAh g^{-1} or mAh cm^{-3}) was calculated by dividing Eq. (3) or (4), respectively, either by mass (g) or geometrical volume (cm^{-3}) of the electrode. For the full cell, geometrical volume or weight of both electrodes was considered. The thickness of the membrane was not taken into account while measuring the volumetric performance. The Energy, E (in J) is calculated using Eq. (1). The Energy in mWh is calculated by Eq. (1) by 3.6. The power, P (in mW) is calculated as:

$$P = \frac{E. \, v}{V},$$ (6)

where, E (J) is the energy of the cell, v (Vs^{-1}) is the scan rate of the CV and V (V) is the cell voltage. Energy and power density was calculated by dividing Eq. (1) or (6), respectively, either by mass (g) or geometrical volume (cm^{-3}) of both electrodes.

2.5.1. Three-electrode cell measurements

For three-electrode cell measurements, an over-capacitive electrode made of activated carbon (YP50) was used as a counter electrode (YP50: PTFE – wt. ratio 95:5, > 5 times the weight of the working electrode), a saturated calomel electrode as a reference (SCE, CHI Instruments), and Celgard membrane 3501 as the separator (Celgard®, > 4 mm diameter). Polished glassy carbon was used as the current collector(s) (CHI Instruments). MnO$_2$, as an active material, was mixed with a conductive carbon additive (AB, Acetylene Black, Alfa Aesar) and binder (polytetrafluoroethylene, PTFE; Sigma Aldrich) in the mass ratio of 75:20:5, respectively. The powders were mixed with a low volume of ethanol and the resulting slurry was heated up to 60 °C while being magnetically stirred to evaporate the solvent. Finally, the paste was rolled to form a homogenous film. The thickness, weight loading and packing density of MnO$_2$ films were ~100 μm, ~12.5 mg cm^{-2} and ~1.28 g cm^{-3}, respectively, and of Ti$_3$C$_2$ films were ~8 μm, ~2.2 mg cm^{-2} and ~2.75 g cm^{-3}, respectively. Both MnO$_2$ and Ti$_3$C$_2$ films were punched into a circular disk shape of 3 mm in diameter and used as working electrodes. The weight of the electrodes was determined using PerkinElmer AD-6 microbalance.

2.5.2. Assembly and electrochemical characterization of the cells

Measurements were carried out using in a Swagelok cell. The cell body was made up of polytetrafluoroethylene. Polished glassy carbon was used as the current collector(s) (CHI Instruments). For comparison of the electrochemical properties of the Ti$_3$C$_2$//α-MnO$_2$ asymmetric supercapacitor, an asymmetric cell of activated carbon (YP-50//YP-50) was assembled using YP-50, Acetylene Black and PTFE in the mass ratio of 75:20:5, respectively. The thickness, weight loading and packing density of YP-50 film were ~50 μm, ~4.5 mg cm^{-2} and ~0.9 g cm^{-3}, respectively. A mass balancing approach was carried out to equilibrate

the charges between the positive and negative electrode [41,42] by:

$$R = \left(\frac{m_+}{m_-}\right) = \left(\frac{C_- \, \Delta V_-}{C_+ \Delta V_+}\right),$$ (5)

where m_+ and m_- represent the mass, C_+ and C_- the capacitance, and ΔV_+ and ΔV_- the potential window of the positive and negative electrode. The *R-value,* from Eq. (5), between the positive and negative carbon electrodes, was ~1.3. For comparative purpose, dimensions of the MnO$_2$ electrode were also adjusted nearly to the thickness and diameter of YP-50 electrodes; with a weight loading of ~9 mg cm^{-2} and a density of ~1.6 g cm^{-3} (~55 μm thick). Ti$_3$C$_2$ films were also adjusted to a thickness of ~10 μm (~3.0 g cm^{-2}, ~3.0 g cm^{-3}). The average mass ratio, R-value, between α-MnO$_2$ and Ti$_3$C$_2$ was ~3.6. Prior to cell assembly, both α-MnO$_2$ (positive) and Ti$_3$C$_2$ (negative) electrodes were pre-cycled in a three-electrode configuration at a scan rate of 5 mV s^{-1} for 5 cycles and then polarised to -0.2 V *vs*. SCE. After the assembly of the precycled electrodes in a Ti$_3$C$_2$//α-MnO$_2$ cell configuration, consecutive voltage-hold tests were implemented to determine the operational cell voltage. To do so, the cell was held at different voltages for a duration of 2 h during which the leakage current was measured. Upper cut-off voltage was determined by the electrochemical potentials of water splitting on glassy carbon (current collector). Impedance behavior of the Ti$_3$C$_2$//α-MnO$_2$ cell was measured in the potentiostatic mode of electrochemical impedance spectroscopy (PEIS) technique at frequencies from 200 kHz to 10 mHz. The amplitude of the applied potential was ± 10 mV. Fits to impedance data using an equivalent circuit were conducted using Zview software.

2.5.3. Self-discharge measurements

Self-discharge in Ti$_3$C$_2$//α-MnO$_2$ and YP-50//YP-50 cells was evaluated by measuring the open circuit voltage of cells after being charged to their optimum voltage at a current density of 10 mA g^{-1}, holding cell voltage for 2 h and then releasing the voltage. For self-discharge investigation of Ti$_3$C$_2$ and α-MnO$_2$ electrodes in the asymmetric cell Ti$_3$C$_2$//α-MnO$_2$ configuration was carried out with the reference incorporated T-shape Swagelok cells. The asymmetric cell of Ti$_3$C$_2$//α-MnO$_2$ was held at 2.2 V for a duration of 25 h. Electrochemical potentials of the Ti$_3$C$_2$ and α-MnO$_2$ electrodes were determined with reference to SCE.

2.5.4. Electrochemical stability measurements

Stability of the asymmetric Ti$_3$C$_2$//α-MnO$_2$ cell was analyzed by using galvanostatic mode of charge-discharge at a current density of 1 A g^{-1} over 10,000 cycles. The applied current density was normalized by the mass of both electrodes. Voltage hold tests were performed for 25 h at the maximum cell voltage (2.2 V) and the response of the leakage current was observed.

3. Results and discussions

2-D Ti$_3$C$_2$ MXene is prepared via the MILD method by etching the layered Ti$_3$AlC$_2$ MAX [37], see methods for details. XRD patterns of Ti$_3$AlC$_2$ MAX and Ti$_3$C$_2$ MXene are shown in Fig. S1 (ESI). The disappearing of MAX peaks (noticeably, (104)) to the benefice of (00l) peaks of the MXene agrees with previous reports [37] and demonstrates efficient leaching of Al from the Ti$_3$AlC$_2$ MAX precursor and itsconversion into Ti$_3$C$_2$ MXene. EDS analysis also confirms the absence of Al on the Ti$_3$C$_2$ MXene film, (Fig. S2b). The transition from a 3-D MAX micrometric particles to a film of MXene made of 2-D nano-flakes induces diffraction peak broadening and, in particular, a shift of (002) peak from 9.48° to 7.16° (2θ) (Fig. 1a). The shift of (002) peak in XRD pattern agrees with the restacked film structure observed in the SEM image (Fig. 1b) and indicates an increase of d-spacing from 9.31 Å to 12.38 Å for the Ti$_3$C$_2$ MXene phase. This is in agreement with the presence of water molecules between the interlayers of MXene [37].
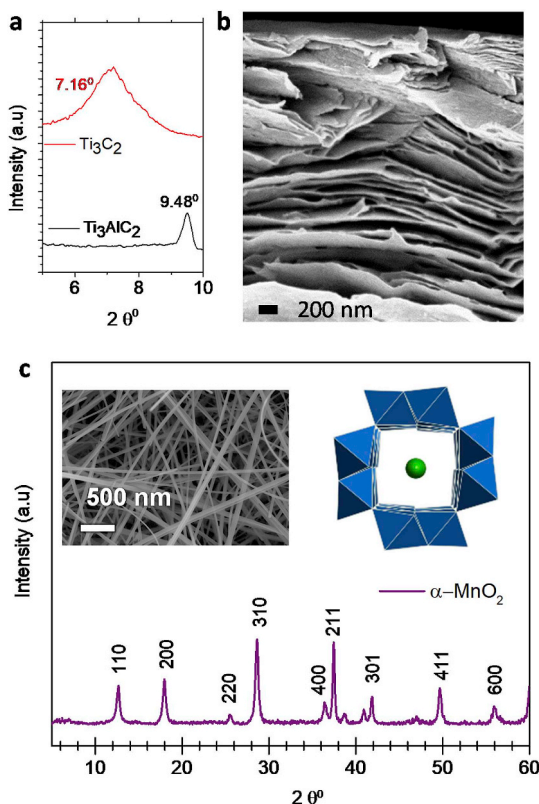
Fig. 1. (a) XRD pattern of Ti_3AlC_2 MAX and Ti_3C_2 MXene focused on 5–10° (2θ) (002) region (extended XRD pattern available in Fig. S1, ESI). **(b)** SEM image of a Ti_3C_2 MXene film after etching, showing layered film morphology (stacked flakes of MXene). **(c)** XRD pattern of α-MnO_2. Inset, left: SEM Image of α-MnO_2, right: Schematic of α-MnO_2 structure (green circle represents intercalated K^+ ions and MnO_2 octahedra are represented in blue).

EDS analysis on the Ti_3C_2 MXene film indicates the presence of F, Cl and O elements, which could be in the form of surface terminal groups with Ti_3C_2 MXene (Fig. S2b).

It is noteworthy that the d-spacing of 12.38 Å in the MXene film is a relatively large interlayer space, which is feasible for the intercalation of either K^+ ions [43] (ionic radii of K^+ ion = 1.37 Å [44]) or solvated $K(H_2O)_{7-x}^+$ ~1.37 - 2.80 Å [44]. The measured resistivity of the Ti_3C_2 MXene film using four probe was 0.541 ± 0.014 mΩcm (See methods), which is in good agreement with the reported values (0.56–0.46 mΩcm [45]).

α-MnO_2 was prepared via hydrothermal method [40]. SEM image shows the morphology of nanowire (Fig. 1c, inset), which is expected to be beneficial for the electrochemical applications as demonstrated in Ref. [46]. The XRD pattern of α-MnO_2, as shown in Fig. 1c, is indexed to tetragonal I4/m phase (JCPDS card # 44-014), which indicates the presence of 1×1 and 2×2 tunnel with an aspect of ~7.0 × 7.0 Å and ~2.3 × 2.3 Å, respectively. Besides, non-existence of intense peaks below 12° (2θ) suggests the absence of a tunnel side larger than two octahedra [46]. A schematic of the tunnel size consisting of two octahedra is shown in Fig. 1c, inset. Notably, the maximal ion radius to be able to access the 2×2 tunnel structure is 1.30 Å, as calculated based on the distance between oxygen-oxygen atoms in tunnel site [29]. This maximal ion radius of α-MnO_2 being closer to the ionic radii of K^+ ion (1.37 Å [44]), which indicates the possibility of intercalation of K^+ ions in α-MnO_2. EDS analysis on the α-MnO_2 samples indicate the presence of K element (Fig. S2c, ESI), which is in agreement with the previous reports [47]. The presence of these stabilizing ions provides an efficient diffusion of the electrolyte ions into the tunnel structure during charging/discharging process [46,47]. The measured resistivity of α-MnO_2 pellets was 295.67 ± 13.3 Ωcm.

In order to highlight the importance of using the water-in-salt electrolyte over conventional aqueous electrolytes, the electrochemical properties of Ti_3C_2 MXene were measured in a conventional 1 m and 21 m potassium acetate based water-in-salt based electrolyte using the cyclic voltammetry (CV) technique in a three-electrode cell configuration. The CV curve of Ti_3C_2 MXene in 1 m at a scan rate of 5 mVs^{-1} shows a capacitive-like profile (Fig. S3a, ESI; CV curves of glassy carbon current collector are shown in Fig. S3b, ESI) with a gravimetric capacity of 21.9 mAhg^{-1} (79 Fg^{-1}). The CV curve also indicates that the negative vertex potential for Ti_3C_2 MXene electrode in 1 m was -1.1 V vs SCE (Potential window: -0.1 V to -1.1 V *vs.* SCE) which shifts to -1.6 V vs SCE when Ti_3C_2 MXene was examined in 21 m potassium acetate water-in-salt electrolyte (Potential window: -0.1 V to -1.6 V *vs.* SCE). This extension of vertex potential with the transition from the conventional to water-in-salt electrolytes is consistent with the recent findings of Tian et al. [27] on the electrochemical behavior of potassium acetate based water-in-salt electrolytes for K^+ ion batteries. Interestingly, the CV curve indicates a capacity value of 32 mAhg^{-1} for Ti_3C_2 MXene in 21 m potassium acetate based water-in-salt electrolyte, which was higher than the value obtained in conventional 1 m of potassium acetate electrolyte (21.9 mAhg^{-1}, 5 mVs^{-1}). This trend is also in agreement with the recent report of Kim et al. [48] in which the rise of capacity in the highly concentrated electrolyte is attributed to the dense accumulation of hydrated cations in the MXene interlayers. Considering the advantage of both wider negative vertex potential and higher capacity for Ti_3C_2 MXene in water-in-salt electrolytes with respect to conventional 1 m, further studies were carried out using super-concentrated electrolyte. Two electrolyte concentrations were investigated: 21 m and 30 m, using Ti_3C_2 MXene films as electrode The plot of log scheme of current over scan rate shows a higher slope for 21 m (0.91) than for 30 m (0.79) (Fig. S4c, ESI). Since the slope of 21 m is closer to 1, it represents capacitance independence over rate with a reversible behavior [43]. This enhanced reversible behavior for the 21 potassium acetate electrolyte is attributed to its higher ionic conductivity (53.6 ± 1.4 mS cm^{-1}) with respect to the conductivity of 30 m potassium acetate electrolyte (27.80 ± 1 mS cm^{-1}, calculated using Eq. (2)). As a whole, the molality of 21 m potassium acetate electrolyte shows better kinetic of insertion/diffusion of K^+ ions within the interlayers of Ti_3C_2 MXene so it was selected as super-concentrated electrolyte for further analysis and device assembly.

The electrochemical properties of Ti_3C_2 MXene and α-MnO_2 were measured by CV technique and the response at a scan rate of 5 mVs^{-1} is shown in Fig. 2. The charge storage of Ti_3C_2 MXene in 21 m of potassium acetate, as calculated from the CV curve using Eq. (4),
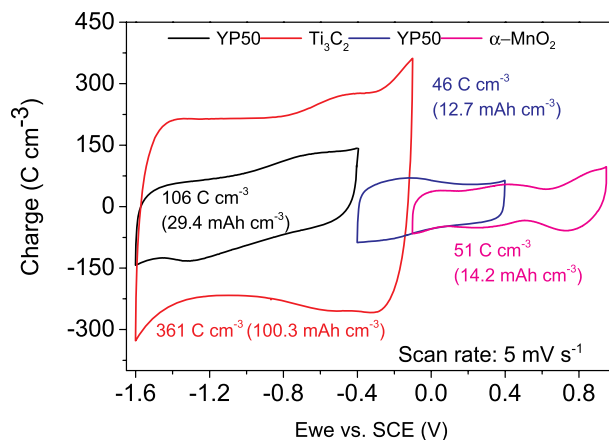

Fig. 2. Cyclic voltammogram of Ti_3C_2 MXene films, YP50 and α-MnO_2 (2×2 MnO_2) individual electrodes in a three-electrode configuration following the potential windows of their respective device (black and blue traces for YP-50//YP-50 and, red and purple traces for Ti_3C_2//α-MnO_2), at scan rate of 5 mV s^{-1} in 21 m potassium acetate electrolyte.

a

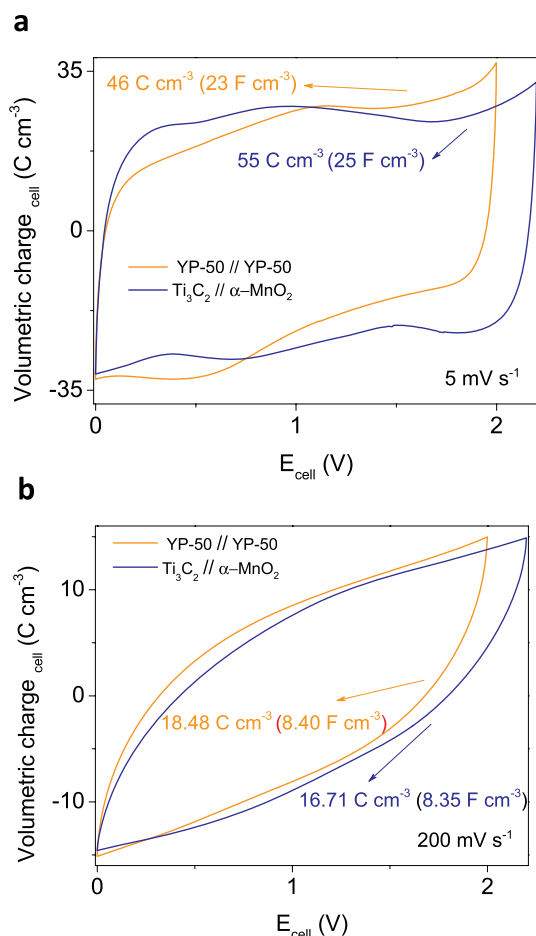## b

Fig. 3. Cyclic voltammograms of the YP-50//YP-50 and Ti$_3$C$_2$//α-MnO$_2$ cells (orange and blue trace, respectively) at **(a)** low rate (5 mV s^{-1}) and **(b)** high rate (200 mV s^{-1}) in 21 m potassium acetate electrolyte.

corresponds to a volummetric capacity of ~100 mAh cm^{-3}. Whereas, the CV curve of α-MnO$_2$ shows a pseudocapacitive performance originating from surface redox reactions [4,29]. This charge storage corresponds to a capacity of ~14 mAh cm^{-3}. Electrochemical analyses also show that the negative potential limit of Ti$_3$C$_2$ MXene is close to -1.6 V *vs.* SCE, whereas α-MnO$_2$ can be cycled up to 0.95 V *vs.* SCE. Convoluting the scanning electrochemical potential window (SPW) of both electrodes gives the possibility to achieve a cell voltage up to 2.55 V. CV curves of 21 m of potassium acetate electrolyte on a glassy carbon indicate that the negative and positive vertex potentials are -1.6 V and 1.1 V *vs.* SCE, respectively (Fig. S5, ESI), which convolutes to a maximum voltage of 2.7 V. However, Voltage-hold tests convey to a different value for the maximum cell voltage. Beyond 2.2 V, the value of leakage current is unstable during the voltage-hold tests (Fig. S6, ESI) which implies cell failure. This failure is caused by the widening of the potential window of α-MnO$_2$ in order to respond the increase of cell voltage (Fig. S7 and Fig. S8, ESI), which leads to the formation of soluble Mn^{2+} species [29]. Considering these analyses, the asymmetric cell of Ti$_3$C$_2$//α-MnO$_2$ was operated between 0 to 2.2 V. The CV curve at a scan rate of 5 mV s^{-1}, as shown by Fig. 3a, demonstrates that the Ti$_3$C$_2$//α-MnO$_2$ cell shows a rectangular shape profile which is typical of capacitive-like charge storage. The galvanostatic charge and discharge curves measured at a current density of 0.25 A g^{-1} (Fig. S9, ESI) show a linear voltage-time response, which also indicates a capacitive behavior of the Ti$_3$C$_2$//α-MnO$_2$ cell.

The Nyquist plot of Ti$_3$C$_2$//α-MnO$_2$ cell and equivalent circuit used for data fitting are shown in Fig. S10 (ESI). Impedance data show a high frequency semicircle with an inclined spike of ~45° at intermediate

frequencies (Fig. S10a, ESI), which terminates in an open circuit or capacitive behavior at even lower frequencies (Fig. S10b, ESI). Impedance data was fitted using a modified version of the Randles circuit (Fig. S10c, ESI), in which the typical double layer capacity (C$_{dl}$) has been substituted by a CPE$_1$ in order to fit the non-ideal high frequency semicircle. Other circuit elements, such as the R$_1$, R$_2$ and Z$_W$ can be correlated to electrolyte resistance, charge-transfer resistance and ionic diffusion across the electrode-electrolyte interface, respectively. This impedance behavior is characteristic of a pseudocapacitor system as previously by Kurra et al. with asymmetric cell of Ti$_3$C$_2$ MXene//RuO$_2$ pseudocapacitors [49]. Besides this, Nyquist plots measured between 1.4 to 2.2 V show a phase angle close to that of 70° at a frequency of 10 mHz (Fig. S10d, ESI), which also illustrates a pseudocapacitive type charge storage behavior as previously demonstrated by Levi et al. in Ti$_3$C$_2$ MXene using an aqueous electrolyte [43].

For comparison with a non-pseudocapacitive cell, an asymmetric supercapacitor based on activated carbon electrodes (YP-50) was also assembled, hereafter referred as YP-50//YP-50 (see methods). The CV curves at 5 mV s^{-1} for both, YP-50//YP-50 and Ti$_3$C$_2$//α-MnO$_2$ cell are shown in Fig. 3a. The response of Ti$_3$C$_2$//α-MnO$_2$ cell corresponds to a capacitance of 25 F cm^{-3} (or capacity of ~15 mAh cm^{-3}), which is close to that of YP-50//YP-50 cell, 23 F cm^{-3} (or capacity of ~13 mAh cm^{-3}, as calculated based on Eqs. (3) and (4)). CV curves at 200 mV s^{-1} in Fig. 3b show resistive behavior for both YP-50//YP-50 and Ti$_3$C$_2$//α-MnO$_2$ cells and the rate decay at $C_{5\,mV\,s^{-1}}/C_{100\,mV\,s^{-1}}$ (Fig. S11, ESI), which measures a value of the capacitance over the scan rate, indicates a similar value (~48%) for both the asymmetric YP-50//YP-50 and Ti$_3$C$_2$//α-MnO$_2$ cells. Comparing these results with the literature, capacitance fade of the asymmetric Ti$_3$C$_2$//α-MnO$_2$ supercapacitor is lower than the existing carbon-MnO$_2$ hybrid capacitor operated using 21 m LiTFSI water-in-salt electrolyte (~17.6%) [23]. The resulting low capacitance decay for the asymmetric supercapacitor is credited to the higher ionic conductivity of 21 m potassium acetate (53.6 ± 1.4 mS cm^{-1}) over 21 m LiTFSI water-in-salt electrolyte (7.14 ± 0.18 mS cm^{-1}, as calculated based on Eq. (2)).

In addition to this, self-discharge measurements were conducted for YP-50//YP-50 and Ti$_3$C$_2$//α-MnO$_2$ cells and results are presented in Fig. 4. In Fig. 4a–f, both cells were charged at different voltages (from 1.5 V to 2.0 V) for 2 h and the percentage of final to initial voltage (VV$_0^{-1}$) was plotted as a function of time or log time. Measurements as a function of time for Ti$_3$C$_2$//α-MnO$_2$ and YP-50//YP-50 in Fig. 4 a and b, respectively, indicate better voltage retention for the asymmetric Ti$_3$C$_2$//α-MnO$_2$ supercapacitor, suggesting a reduced charge-redistribution compared to YP-50//YP-50 cell. Analyses of self-discharge in log time within the initial period (< 100 s), Fig. 4 c and d, show a linear drop after a plateau, whereas voltage decays linearly for the intermediate period (> 100 s), Fig. 4 e and f. This behavior suggests the presence of an activation-controlled Faradaic mechanism in both cells at that time frames. The presence of an activation-controlled Faradaic process in YP-50//YP-50 cell is likely due to the oxidation/reduction of carbon functionalities, as previously observed by Black et al. [50,51]. However, an activation-controlled Faradaic process and restricted charge-redistribution behavior in the Ti$_3$C$_2$//α-MnO$_2$ cell is related to its pseudocapacitive behavior, as previously reported with self-discharge analysis of the pseudocapacitive materials MnO$_2$ and RuO$_2$ by Andreas et al. [51,52].

Unlike in standard aqueous electrolytes [52], YP-50//YP-50 in water-in-salt electrolyte exhibits much higher time response (Fig. 5a). Such low self-discharge (> few mins) is attributed to the diffusion limitation of charges at the interface between the electrolyte and electrode (fluid-solid interface, FSI [53]), which can be emphasized by the decay of voltage with $t^{-1/2}$ [54]. The deviation from linear decay of voltage with $t^{-1/2}$ in YP-50//YP-50, Fig. 5a inset, and in Ti$_3$C$_2$//α-MnO$_2$, Fig. 5b inset, confirms the existence of a diffusion limitation [55] which is attributed to the higher viscosity of water-in-salt (> 10 mPa s^{-1} [25]) compared to standard aqueous electrolytes (< 2 mPa s^{-1} [56]). The use

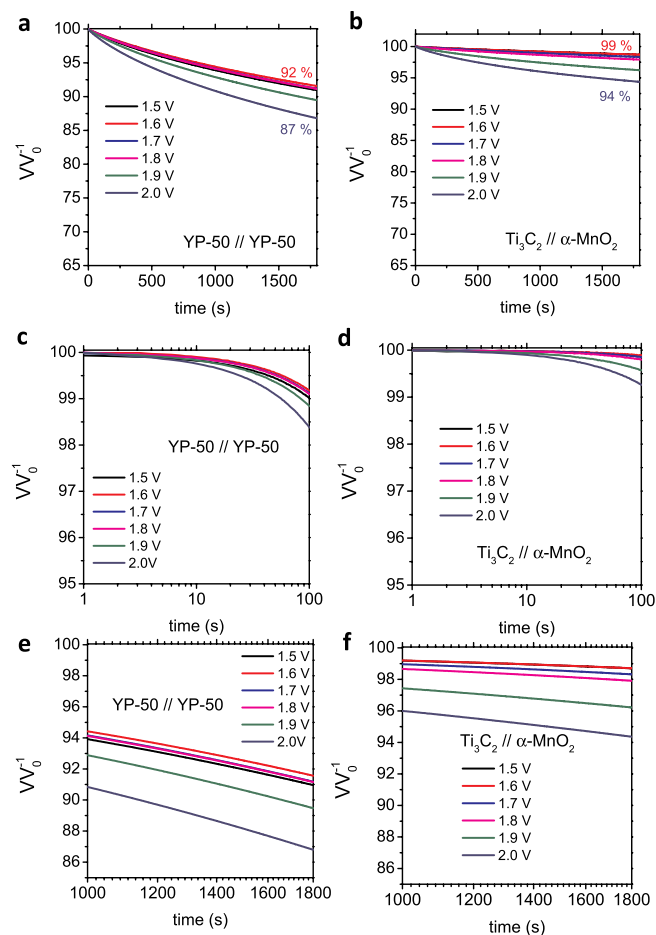**Fig. 4.** Self-discharge of **(a)** YP-50//YP-50 and **(b)** Ti$_3$C$_2$/α-MnO$_2$ cells at different charging voltages. The decay of the open-circuit voltage (E$_{cell}$) was evaluated after consecutively charging the cells from 1.5 to 2.0 V and holding E$_{cell}$ for 2 h. The plot between voltage decay versus log in time for **(c)** YP-50// YP-50 and **(d)** Ti$_3$C$_2$/α-MnO$_2$ cells and the plot between voltage decay and versus log in time for **(e)** YP-50//YP-50 and **(f)** Ti$_3$C$_2$/α-MnO$_2$ cells to observed the to observed the charge-redistribution and activation controlled self-discharge reaction.

Fig. 5. (a) Self-discharge of YP-50//YP-50 and Ti$_3$C$_2$//α-MnO$_2$ cells. The decay of the open circuit voltage (E$_{cell}$) was evaluated during 8-14 h, after consecutively charging the cells to the maximum voltage 2.2 V and 2.0 V, respectively) at 10 mA g^{-1} and holding E$_{cell}$ max. for 2 h. **(b)** Potential decay of individual electrodes of the Ti$_3$C$_2$//α-MnO$_2$ cell measured (with respect to SCE reference electrode) after holding the maximum cell voltage for 25 h. **Inset figures**: The decay behaviour as the function of $t^{-1/2}$, where t represents the decay time under open circuit potetial.

of electrolytes with high viscosities constraints the redistribution of charges at the FSI [54,55]. In the initial 30,000 s of self-discharge, the voltage of Ti$_3$C$_2$//α-MnO$_2$ cell fades from 2.2 V to ~1.5 V, whereas the voltage of YP-50//YP-50 reduces from 2.0 V to ~1.3 V. These decays can be quantified to ~68% and 65% of their maximum cell voltage, respectively. Interestingly, for the asymmetric supercapacitor to reach an analogous self-discharge of ~65% as in YP-50//YP-50 cell, extra 20,500 s are needed (almost 1.7 times longer) which indicates a significantly slower self-discharge.

Monitoring the electrochemical behavior of each electrode during the self-discharge of the Ti$_3$C$_2$//α-MnO$_2$ suggests that the voltage decay of Ti$_3$C$_2$ is initially faster, but then becomes slower after 10,000 s compared to α-MnO$_2$ (Fig. 5b). Diffusion limitation occurs at both electrodes, Fig. 5b inset, however voltage profiles as a function of $t^{-1/2}$ are significantly different between Ti$_3$C$_2$ and α-MnO$_2$ electrodes. The mechanism behind this phenomenon is still unclear and further investigations are required. However, recent experiments by Levi et al. and Ren et al. [43,57] have shown faster ion desorption from Ti$_3$C$_2$ surface sites, followed by slower desorption of trapped ions within the shallow adsorption sites of Ti$_3$C$_2$ MXene. We hypothesize that the
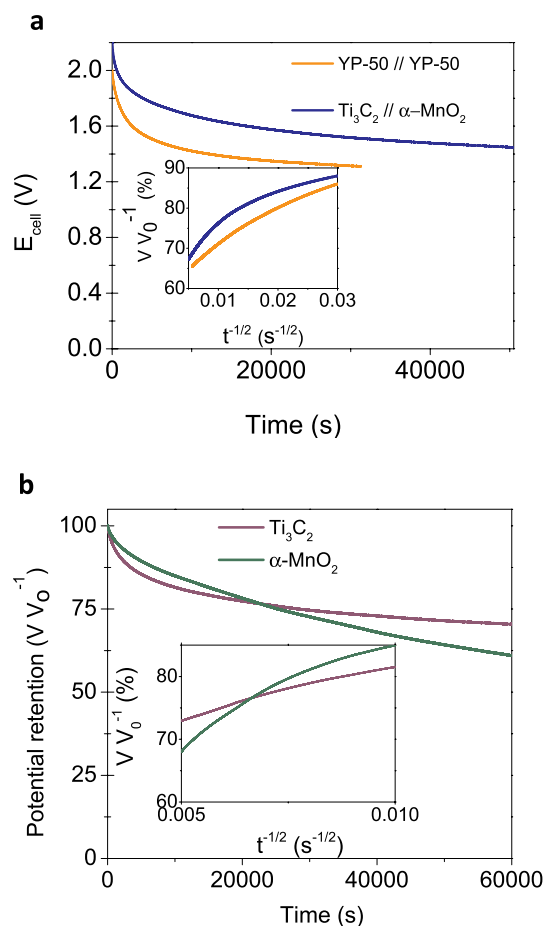
difference of desorption rates at the surface and shallow sites allow Ti$_3$C$_2$ MXene to show a two-step voltage decay during the self-discharge test. Whereas fast ion removal capacity test of K$^+$ ions from α-MnO$_2$, as shown by Bylan et al. during the desalination process [46], allows the α-MnO$_2$ to show high voltage decay during the self-discharge analysis.

As a whole, self-discharge studies suggest that different mechanisms play a role depending on the time frame. On initial and intermediate periods of time, voltage versus log time plots Fig. 4 follow the expected behavior of an activation-controlled Faradaic mechanism and, for studies conducted during long periods of time, Fig. 5, voltage profiles in square root time deviate from linearity in agreement with previous work [55] involving electrolytes with high viscosity, which indicates a diffusion-controlled self-discharge mechanism. Indeed more experiments are necessary to completely characterize the self-discharge behavior of Ti$_3$C$_2$//α-MnO$_2$ cell, for instance, self-discharge as float current measurements and as a function of temperature. We aim to continue this type of investigations on the Ti$_3$C$_2$//α-MnO$_2$ system and others in the near future.

Lastly, long-term cycling tests were performed to determine Ti$_3$C$_2$// α-MnO$_2$ cell stability. Long-term cycling test at a current density of

a

b

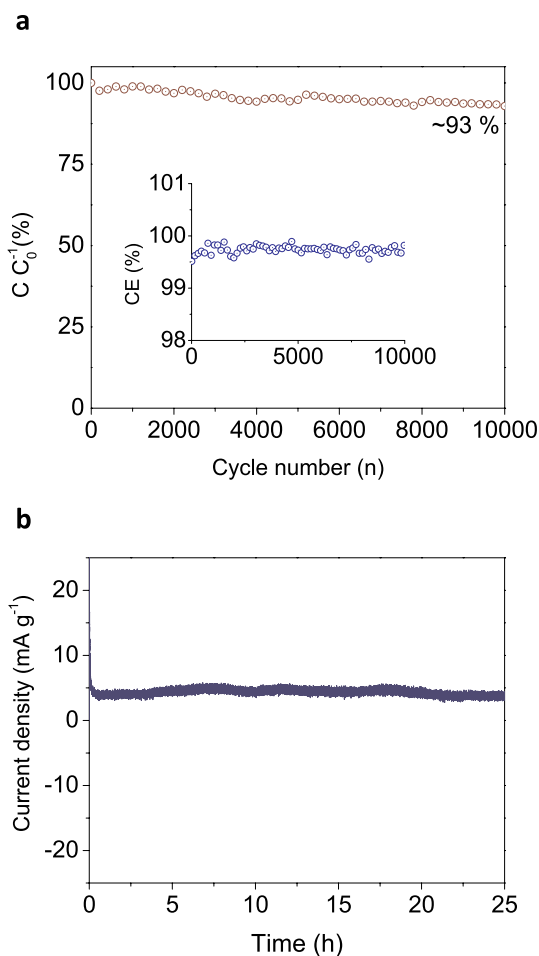**Fig. 6.** Stability analysis of the $Ti_3C_2//\alpha$-MnO_2 cell. **(a)** Capacitance retention, evaluated through long term galvanostatic charge discharge at $1\,A\,g^{-1}$. **Inset figure:** Columbic efficiency (CE) during long term cycling. **(b)** Observed leakage current during the hold tests for 25 h at a cell voltage of 2.2 V. Current density applied **(a)** and measured **(b)** are considered with respect to the mass of both electrodes.

$1\,A\,g^{-1}$ indicates good capacitance retention of ~93% over 10,000 cycles, Fig. 6a, with a columbic efficiency ranging between 99.5 to 99.9% (Fig. 6a, inset). Stability analysis via voltage hold tests at 2.2 V (Fig. 6b), shows a stable leakage current and the cell is able to withstand a current response of $\sim 4 \pm 1.5\,mA\,g^{-1}$ for 25 h. CV curves measured before and after voltage hold tests indicate capacitance retention of 91.64% (Fig. S12, ESI). Also, these CV curves show a small voltage shift for the reductive hump, *i.e.* 1.83 to 1.88 V, which occurs due to the shift in the electrochemical potential window of Ti_3C_2 and α-

MnO_2 towards positive polarization (Fig. S13, ESI). These results prove that our asymmetric $Ti_3C_2//\alpha$-MnO_2 supercapacitor has a very good electrochemical stability. Besides, capacitance retention as a function of cycles is significantly higher (~93%) than the one obtained for recently reported asymmetric supercapacitors, as summarized in Table 1. The stability features are better than the existing carbon//MnO_2 asymmetric cell based on water-in-salt electrolytes. In such systems, rapid decays occur within 5000 cycles [23,28] (< 50%, Table 1). In addition, the volummetric energy density of $Ti_3C_2//\alpha$-MnO_2 cell (16.80 mWh cm^{-3} at 0.13 W cm^{-3}) is ~32% higher than of YP-50//YP-50 cell (12.77 mWh cm^{-3} at 0.11 W cm^{-3}). The Ragone plot (Fig. S14, ESI), which shows the relationship between the volumetric energy and power density, also indicates a higher volumetric energy and power densities for the $Ti_3C_2//\alpha$-MnO_2 cell when compared to the YP-50//YP-50 cell. The observed volumetric energy density of $Ti_3C_2//\alpha$-MnO_2 cell (16.80 mWh cm^{-3} at 137 mW cm^{-3}) is higher than the existing supercapacitors based on water-in-salt electrolytes, such as and AC//MnO_2 in 21 m Li-TFSI [23] (10 mWh cm^{-3} at 44 mW cm^{-3} mWh cm^{-3}), AC//AC in 7 m Li-TFSI [21] (6 mWh cm^{-3} at 49 mW cm^{-3}) and AC//AC cell in 31 m Li-TFSI (8 mWh cm^{-3} at 57 mW cm^{-3}).These results are promising and support the use of asymmetric supercapacitors, such as this $Ti_3C_2//\alpha$-MnO_2 configuration, in applications where the volumetric energy density are required.

4. Conclusions

We assembled an asymmetric cell with a potassium acetate-based water-in-salt electrolyte, where 2D titanium carbide MXene (Ti_3C_2) and manganese oxide (α-MnO_2) were used as a negative and positive electrode, respectively. The high ionic conductivity of the selected potassium acetate water-in-salt electrolyte concentration, i.e. 21 m, enables the asymmetric cell to demonstrate less capacitance fade upon increasing scan rates (~48%) than the asymmetric supercapacitors operated in fluorinated-imide based water-in-salt electrolytes (~17.6%). Furthermore, the asymmetric cell also demonstrates an exceptional electrochemical stability (> 90%) during voltage-hold test and 10,000 cycles, when compared to existing asymmetric supercapacitors using water-in-salt electrolytes (50% or less after 5000 cycles). Due to pseudocapacitive charge storage mechanism and the use of a super concentrated electrolyte, the asymmetric $Ti_3C_2//\alpha$-MnO_2 cell shows slower self-discharge, analogous capacitance and a ~32% increase on volumetric energy density with respect to activated carbon-based supercapacitor. The asymmetric device is, therefore, promising for applications in which high volumetric energy density (high voltage) is required. It is worth to mention that the cell assembly approach herein presented can be extended to other existing MXene phases to built new high-voltage asymmetric supercapacitors.

Competing financial interests

The authors declare no competing financial interests.

Table 1

Comparison of the stability of the pseudocapacitor presented in this work with other hybrid cells functioning with a water-in-salt electrolyte.

Cell type	Charging Mechanism	Electrolyte salt[d]	Capacitance Decay (Cycles)	Hold Tests- Leakage current (mA g^{-1}, cell)	Reference
C-MnO_2[a]	EDLC($-$)/Pseduocapacitive($+$)	LiTFSI	~50% (5,000)	-	[23]
Li-MnO_2[b]	Plating-deplating($-$)/Pseduocapacitive($+$)	LiTFSI	< 25% (5,000)	-	[28]
Ti_3C_2- α-MnO_2[c]	Pseduocapacitive($-$)/Pseduocapacitive($+$)	KAc	~96% (5,000) ~93% (10,000)	~4.0 $\pm$ 1.5 (25 h)	Present work

[a] **Black pearl carbon** (active material: 9.7 mg cm^{-2})/amorphous MnO_2 (active material: 2.9 mg cm^{-2}).
[b] **Lithium** (unknown weight)/MnO_2 (active material: 200 μg cm^{-2}).
[c] **Ti_3C_2** (loading ~3.0 g cm^{-2}, ~10 μm thick, density ~3.0 g cm^{-3}) and **α-MnO_2** (loading ~9 mg cm^{-2}, density ~1.6 g cm^{-3}, ~55 thick).
[d] **Concentration**: 21 m (mol kg^{-1}); LiTFSI: lithium bis(trifluromethane)-sulfonimide; KAc: potassium acetate.

Data availability

Data associated with this article is available from the corresponding author on reasonable request.

Acknowledgments

Appendix A. Supplementary data

Supplementary data to this article can be found online at https:// doi.org/10.1016/j.nanoen.2019.103961.

References

[1] P. Simon, Y. Gogotsi, B. Dunn, Where do batteries end and supercapacitors begin? Science 343 (2014) 1210–1211, https://doi.org/10.1126/science.1249625.

[2] M.R. Lukatskaya, B. Dunn, Y. Gogotsi, Multidimensional materials and device architectures for future hybrid energy storage, Nat. Commun. 7 (2016) 12647, https://doi.org/10.1038/ncomms12647.

[3] V. Augustyn, P. Simon, B. Dunn, Pseudocapacitive oxide materials for high-rate electrochemical energy storage, Energy Environ. Sci. 7 (2014) 1597–1614, https:// doi.org/10.1039/c3ee44164d.

[4] Y. Gogotsi, R.M. Penner, Energy storage in nanomaterials – capacitive, pseudocapacitive, or battery-like? ACS Nano 12 (2018) 2081–2083, https://doi.org/10. 1021/acsnano.8b01914.

[5] T. Brousse, D. Bélanger, J.W. Long, To Be or not to Be pseudocapacitive? J. Electrochem. Soc. 162 (2015) A5185–A5189, https://doi.org/10.1149/2. 0201505jes.

[6] N. Goubard-Bretesché, O. Crosnier, F. Favier, T. Brousse, Improving the volumetric energy density of supercapacitors, Electrochim. Acta 206 (2016) 458–463, https:// doi.org/10.1016/j.electacta.2016.01.171.

[7] P.Y. Chan, Nanomaterials for electrochemical capacitor, Nanomater. Energy Devices, Springer Berlin Heidelberg, Berlin, Heidelberg, 2017, pp. 218–246, , https://doi.org/10.1201/9781315153445.

[8] Y. Gogotsi, P. Simon, True performance metrics in electrochemical energy storage, Science 334 (2011) 917–918, https://doi.org/10.1126/science.1213003.

[9] J.P. Zheng, Hydrous ruthenium oxide as an electrode material for electrochemical capacitors, J. Electrochem. Soc. 142 (1995) 2699, https://doi.org/10.1149/1. 2050077.

[10] B.E. Conway, The electrochemical behavior of ruthenium oxide (RuO_2) as a material for electrochemical capacitors, Electrochem. Supercapacitors, Springer US, Boston, MA, 2013, pp. 259–297, , https://doi.org/10.1007/978-1-4757-3058-6_11.

[11] O. Crosnier, N. Goubard-Bretesché, G. Buvat, L. Athouël, C. Douard, P. Lannelongue, F. Favier, T. Brousse, Polycationic oxides as potential electrode materials for aqueous-based electrochemical capacitors, Curr. Opin. Electrochem. 9 (2018) 87–94, https://doi.org/10.1016/j.coelec.2018.05.005.

[12] A.J. Perez, R. Beer, Z. Lin, E. Salager, P.L. Taberna, A.M. Abakumov, P. Simon, J.M. Tarascon, Proton ion exchange reaction in Li_3IrO_4: a way to new $H_{3+x}IrO_4$ phases electrochemically active in both aqueous and nonaqueous electrolytes, Adv. Energy Mater. 8 (2018) 1702855, https://doi.org/10.1002/aenm.201702855.

[13] G. Ghodbane, J.L. Pascal, F. Favier, Microstructural effects on charge-storage properties in MnO_2-based electrochemical supercapacitors, ACS Appl. Mater. Interfaces 1 (2009) 1130–1139, https://doi.org/10.1021/am900094e.

[14] H.Y. Lee, J.B. Goodenough, Ideal supercapacitor behavior of amorphous $V_2O_5 \cdot nH_2O$ in potassium chloride (KCl) aqueous solution, J. Solid State Chem. 148 (1999) 81–84, https://doi.org/10.1006/jssc.1999.8367.

[15] N.L. Wu, Nanocrystalline oxide supercapacitors, Mater. Chem. Phys. 75 (2002) 6–11, https://doi.org/10.1016/S0254-0584(02)00022-6.

[16] N. Goubard-Bretesché, O. Crosnier, C. Payen, F. Favier, T. Brousse, Nanocrystalline $FeWO_4$ as a pseudocapacitive electrode material for high volumetric energy density supercapacitors operated in an aqueous electrolyte, Electrochem. Commun. 57 (2015) 61–64, https://doi.org/10.1016/j.elecom.2015.05.007.

[17] P. Lannelongue, S. Le Vot, O. Fontaine, M.T. Sougrati, O. Crosnier, T. Brousse, F. Favier, Investigation of $Ba_{0.5}Sr_{0.5}Co_xFe_{1-x}O_{3-\delta}$ as a pseudocapacitive electrode material with high volumetric capacitance, Electrochim. Acta 271 (2018) 677–684, https://doi.org/10.1016/j.electacta.2018.03.173.

[18] S.L. Kuo, N.L. Wu, Electrochemical capacitor of $MnFe_2O_4$ with NaCl electrolyte, Electrochem. Solid State Lett. 8 (2005) A495, https://doi.org/10.1149/1.2008847.

[19] M. Abdollahifar, S.S. Huang, Y.H. Lin, Y.C. Lin, B.Y. Shih, H.S. Sheu, Y.F. Liao, N.L. Wu, High-performance carbon-coated $ZnMn_2O_4$ nanocrystallite supercapacitors with tailored microstructures enabled by a novel solution combustion method, J. Power Sources 378 (2018) 90–97, https://doi.org/10.1016/j.jpowsour. 2017.12.022.

[20] N. Goubard-Bretesché, O. Crosnier, G. Buvat, F. Favier, T. Brousse, Electrochemical study of aqueous asymmetric $FeWO_4/MnO_2$ supercapacitor, J. Power Sources 326 (2016) 695–701, https://doi.org/10.1016/j.jpowsour.2016.04.075.

[21] P. Lannelongue, R. Bouchal, E. Mourad, C. Bodin, M. Olarte, S. le Vot, F. Favier, O. Fontaine, "Water-in-Salt" for supercapacitors: a compromise between voltage, power density, energy density and stability, J. Electrochem. Soc. 165 (2018) A657–A663, https://doi.org/10.1149/2.0951803jes.

[22] L. Suo, O. Borodin, T. Gao, M. Olguin, J. Ho, X. Fan, C. Luo, C. Wang, K. Xu, "Water-in-salt" electrolyte enables high-voltage aqueous lithium-ion chemistries, Science 350 (2015) 938–943, https://doi.org/10.1126/science.aab1595.

[23] A. Gambou-Bosca, D. Bélanger, Electrochemical characterization of MnO_2-based composite in the presence of salt-in-water and water-in-salt electrolytes as electrode for electrochemical capacitors, J. Power Sources 326 (2016) 595–603, https://doi. org/10.1016/j.jpowsour.2016.04.088.

[24] D.P. Leonard, Z. Wei, G. Chen, F. Du, X. Ji, Water-in-Salt electrolyte for potassium-ion batteries, ACS Energy Lett 3 (2018) 373–374, https://doi.org/10.1021/ acsenergylett.8b00009.

[25] M.R. Lukatskaya, J. Feldblyum, D.G. Mackanic, F. Lissel, D.L. Michels, Y. Cui, Z. Bao, Concentrated mixed cation acetate "Water-in-Salt" solutions as green and low cost high voltage electrolytes for aqueous batteries, Energy Environ. Sci. (2018), https://doi.org/10.1039/C8EE00833G.

[26] T. Brousse, M. Toupin, R. Dugas, L. Athouël, O. Crosnier, D. Bélanger, Crystalline MnO_2 as possible alternatives to amorphous compounds in electrochemical supercapacitors, J. Electrochem. Soc. 153 (2006) A2171, https://doi.org/10.1149/1. 2352197.

[27] Z. Tian, W. Deng, X. Wang, C. Liu, C. Li, J. Chen, M. Xue, R. Li, F. Pan, Superconcentrated aqueous electrolyte to enhance energy density for advanced supercapacitors, Funct. Mater. Lett. 10 (2017) 1750081, https://doi.org/10.1142/ s1793604717500813.

[28] M. Zhang, S. Makino, D. Mochizuki, W. Sugimoto, High-performance hybrid supercapacitors enabled by protected lithium negative electrode and "water-in-salt" electrolyte, J. Power Sources 396 (2018) 498–505, https://doi.org/10.1016/j. jpowsour.2018.06.037.

[29] M.J. Young, A.M. Holder, S.M. George, C.B. Musgrave, Charge storage in cation incorporated α-$MnO2$, Chem. Mater. 27 (2015) 1172–1180, https://doi.org/10. 1021/cm503544e.

[30] T. Brousse, D. Bélanger, A hybrid Fe_3O_4-MnO_2 capacitor in mild aqueous electrolyte, Electrochem. Solid State Lett. 6 (2003) A244, https://doi.org/10.1149/1. 1614451.

[31] T. Brousse, M. Toupin, D. Bélanger, A hybrid activated carbon-manganese dioxide capacitor using a mild aqueous electrolyte, J. Electrochem. Soc. 151 (2004) A614, https://doi.org/10.1149/1.1650835.

[32] T. Brousse, P.L. Taberna, O. Crosnier, R. Dugas, P. Guillemet, Y. Scudeller, Y. Zhou, F. Favier, D. Bélanger, P. Simon, Long-term cycling behavior of asymmetric activated carbon/MnO_2 aqueous electrochemical supercapacitor, J. Power Sources 173 (2007) 633–641, https://doi.org/10.1016/j.jpowsour.2007.04.074.

[33] D. Bélanger, T. Brousse, J.W. Long, A survey on dependability in body area networks, Manganese Oxides Batter. Mater. Make Leap to Electrochem. Capacit. 17 (2008) 49–52, https://doi.org/10.1109/ISMICT.2011.5759786.

[34] J.W. Long, D. Bélanger, T. Brousse, W. Sugimoto, M.B. Sassin, O. Crosnier, Asymmetric electrochemical capacitors-Stretching the limits of aqueous electrolytes, MRS Bull. 36 (2011) 513–522, https://doi.org/10.1557/mrs.2011.137.

[35] M. Naguib, Y. Gogotsi, Synthesis of two-dimensional materials by selective extraction, Acc. Chem. Res. 48 (2015) 128–135, https://doi.org/10.1021/ar500346b.

[36] M. Naguib, M. Kurtoglu, V. Presser, J. Lu, J. Niu, M. Heon, L. Hultman, Y. Gogotsi, M.W. Barsoum, Two-dimensional nanocrystals produced by exfoliation of Ti_3AlC_2, Adv. Mater. 23 (2011) 4248–4253, https://doi.org/10.1002/adma.201102306.

[37] M. Alhabeb, K. Maleski, B. Anasori, P. Lelyukh, L. Clark, S. Sin, Y. Gogotsi, Guidelines for synthesis and processing of two-dimensional titanium carbide ($Ti_3C_2T_x$ MXene), Chem. Mater. 29 (2017) 7633–7644, https://doi.org/10.1021/ acs.chemmater.7b02847.

[38] N. Shpigel, M.D. Levi, S. Sigalov, T.S. Mathis, Y. Gogotsi, D. Aurbach, Direct assessment of nanoconfined water in 2D Ti_3C_2 electrode interspaces by a surface acoustic technique, J. Am. Chem. Soc. 140 (2018) 8910–8917, https://doi.org/10. 1021/jacs.8b04862.

[39] A. Sugahara, Y. Ando, S. Kajiyama, K. Yazawa, K. Gotoh, M. Otani, M. Okubo, A. Yamada, Negative dielectric constant of water confined in nanosheets, Nat. Commun. 10 (2019) 850, https://doi.org/10.1038/s41467-019-08789-8.

[40] B.W. Byles, N.K.R. Palapati, A. Subramanian, E. Pomerantseva, The role of electronic and ionic conductivities in the rate performance of tunnel structured manganese oxides in Li-ion batteries, Apl. Mater. 4 (2016) 046108, https://doi.org/10. 1063/1.4948272.

[41] S. Vaquero, J. Palma, M. Anderson, R. Marcilla, Mass-balancing of electrodes as a strategy to widen the operating voltage window of carbon/carbon supercapacitors in neutral aqueous electrolytes, Int. J. Electrochem. Sci. 8 (2013) 10293–10307.

[42] L. Demarconnay, E. Raymundo-Piñero, F. Béguin, Adjustment of electrodes potential window in an asymmetric carbon/MnO_2 supercapacitor, J. Power Sources 196 (2011) 580–586, https://doi.org/10.1016/j.jpowsour.2010.06.013.

[43] M.D. Levi, M.R. Lukatskaya, S. Sigalov, M. Beidaghi, N. Shpigel, L. Daikhin, D. Aurbach, M.W. Barsoum, Y. Gogotsi, Solving the capacitive paradox of 2D MXene using electrochemical quartz-crystal admittance and in situ electronic conductance measurements, Adv. Energy Mater. 5 (2015) 1–11, https://doi.org/10.1002/aenm. 201400815.

[44] W.M. Haynes, D.R. Lide, T.J. Bruno, Handbook of Chemistry and Physics, 93rd ed., CRC Press., Boca Raton, 2018, https://doi.org/10.1201/9781315380476.

[45] F.M. Römer, U. Wiedwald, T. Strusch, J. Halim, E. Mayerberger, M.W. Barsoum, M. Farle, Controlling the conductivity of Ti_3C_2 MXenes by inductively coupled oxygen and hydrogen plasma treatment and humidity, RSC Adv. 7 (2017) 13097–13103, https://doi.org/10.1039/c6ra27505b.

[46] B.W. Byles, D.A. Cullen, K.L. More, E. Pomerantseva, Tunnel structured manganese oxide nanowires as redox active electrodes for hybrid capacitive deionization, Nano Energy 44 (2018) 476–488, https://doi.org/10.1016/j.nanoen.2017.12.015.

[47] B.W. Byles, E. Pomerantseva, Effect of manganese oxide crystal tunnel size on Li-ion and Na-ion battery performance, Proc. SPIE 9924 (2016) 992406, https://doi.org/10.1117/12.2238638.

[48] K. Kim, Y. Ando, A. Sugahara, S. Ko, Y. Yamada, M. Otani, M. Okubo, A. Yamada, Dense charge accumulation in MXene with hydrate melt electrolyte, Chem. Mater. (2019), https://doi.org/10.1021/acs.chemmater.9b01334 acs.chemmater. 9b01334.

[49] Q. Jiang, N. Kurra, M. Alhabeb, Y. Gogotsi, H.N. Alshareef, All Pseudocapacitive MXene-RuO_2 Asymmetric Supercapacitors 1703043 (2018), pp. 1–10, https://doi.org/10.1002/aenm.201703043.

[50] J. Black, H.A. Andreas, Effects of charge redistribution on self-discharge of electrochemical capacitors, Electrochim. Acta 54 (2009) 3568–3574, https://doi.org/10.1016/j.electacta.2009.01.019.

[51] H.A. Andreas, J.M. Black, A.A. Oickle, Self-discharge in manganese oxide electrochemical capacitor electrodes in aqueous electrolytes with comparisons to faradaic and charge redistribution models, Electrochim. Acta 140 (2014) 116–124, https://doi.org/10.1016/j.electacta.2014.03.104.

[52] H.A. Andreas, Self-discharge in electrochemical capacitors: a perspective article, J. Electrochem. Soc. 162 (2015) A5047–A5053, https://doi.org/10.1149/2.0081505jes.

[53] A.C. Forse, C. Merlet, J.M. Griffin, C.P. Grey, New perspectives on the charging mechanisms of supercapacitors, J. Am. Chem. Soc. 138 (2016) 5731–5744, https://doi.org/10.1021/jacs.6b02115.

[54] A. Laheäär, A. Arenillas, F. Béguin, Change of self-discharge mechanism as a fast tool for estimating long-term stability of ionic liquid based supercapacitors, J. Power Sources 396 (2018) 220–229, https://doi.org/10.1016/j.jpowsour.2018.06.009.

[55] E. Mourad, L. Coustan, P. Lannelongue, D. Zigah, A. Mehdi, A. Vioux, S.A. Freunberger, F. Favier, O. Fontaine, Biredox ionic liquids with solid-like redox density in the liquid state for high-energy supercapacitors, Nat. Mater. (2016), https://doi.org/10.1038/nmat4808.

[56] A. Boisset, L. Athouël, J. Jacquemin, P. Porion, T. Brousse, M. Anouti, Comparative performances of birnessite and cryptomelane MnO_2 as electrode material in neutral aqueous lithium salt for supercapacitor application, J. Phys. Chem. C 117 (2013) 7408–7422, https://doi.org/10.1021/jp3118488.

[57] C.E. Ren, M. Alhabeb, B.W. Byles, M.Q. Zhao, B. Anasori, E. Pomerantseva, K.A. Mahmoud, Y. Gogotsi, Voltage-gated ions sieving through 2D MXene $Ti_3C_2T_x$ membranes, ACS Appl. Nano Mater. 1 (2018) 3644–3652, https://doi.org/10.1021/acsanm.8b00762.

Bryan W. Byles received his bachelor's degree in Materials Science and Engineering from Rutgers University in 2013, followed by his Ph.D. from Drexel University in the Department of Materials Science and Engineering in 2018. He worked under Dr. Ekaterina Pomerantseva, where his research focused on investigating the performance of tunnel structured manganese oxides for electrochemical energy and water treatment applications.

Dr. David Pinto received his Engineering and PhD degrees in Materials Science (Physic and Chemistry of Materials) from University Pierre and Marie Curie (Paris, France). He was a post-doctoral researcher at the Laboratoire Chimie de la Matière Condensée de Paris (France) and at the Drexel Nanomaterials Institute (Philadelphia, PA, USA). His research interests and activity focus on materials for energy storage devices, in term of engineering and physico-chemistry.

José Miguel Delgado Galindo received his Bachelors in Physics and Masters in Nanoscience at the University of Barcelona. He is currently a PhD student at the Barcelona University in the Energy Storage and Harvesting department at the Catalonia Institute for Energy Research (IREC), where his research interest involves understanding the interface between electrode and water-in-salt electrolytes for electrochemical supercapacitors.

Dr. Jordi Jacas Biendicho obtained his PhD in Materials science and Engineering at Sheffield University working on the electrical and electrochemical characterization of electrode materials for Li-ion batteries. During his Postdoc, he developed new tools to characterize batteries in-situ using neutron diffraction at Stockholm University and the ISIS neutron facility. Dr. Jordi Jacas is currently a consolidated researcher in the Energy Storage group at the Catalonia Institute for Energy Research (IREC) working on different technologies ranging from supercapacitors to flow batteries.

Hemesh Avireddy is currently a researcher at the Catalonia Institute for Energy Research (Spain). He received his Ph.D in Nanosciences and Nanotechnology from the University of Barcelona in 2019. He has been as a visiting researcher at Institut des Matériaux Jean Rouxel-Polytech Nantes (France) and A. J. Drexel Nanomaterials Institute, Drexel University (US). His research activities are focused on the electrode assembly and architecture for the electrochemical energy storage devices.

Xuehang Wang is currently a postdoc researcher in A. J. Drexel Nanomaterials Institute, Drexel University, US. She received her Ph.D. in chemical engineering from Norwegian University of Science and Technology, Norway in 2016. Her research interests focus on the charge mechanism of the energy storage devices, especially the electrolyte transportation at electrode-electrolyte interphases of 2D MXenes and various carbon materials.

Dr. Cristina Flox is a scientific researcher at Aalto University. She received her PhD degree in Chemistry from Universitat de Barcelona (2008). Her research interest are focused on the design and synthesis of functional nanomaterials for electrochemical water splitting (HER/OER) and storage applications (redox flow batteries, and supercapacitor).

Ekaterina Pomerantseva received a Ph.D. degree in Solid-State Chemistry in 2007 from Moscow State University. Prior to joining Drexel Faculty in September 2013, she held postdoctoral appointments at the University of Maryland (2010–2013) and at the University of Waterloo (2009–2010). She has co-authored over 60 journal papers. Her research interests lie in the development and characterization of novel nanostructured materials for energy storage and water treatment with the goal to better understand electrochemical processes at nanoscale. She leads the Materials Electrochemistry Group, whose research is focused on design and application of the chemical synthesis methods to obtain materials with the desired structure and electrochemical properties.

Dr. Olivier Crosnier is an assistant professor at the University of Nantes (France) since 2007. He is a researcher at Institut des Matériaux Jean Rouxel (IMN). His research focuses on materials for electrochemical energy storage with particular emphasis on innovative and/or modified materials for electrochemical capacitors and related devices. He has worked on electrode materials (both positive and negative), for supercapacitors as well as Lithium and Sodium-ion batteries, from synthesis, functionalization to materials characterization. He completed his PhD in 2001 and worked as a postdoctoral fellow at the University of Waterloo (Canada) and ICMCB (Bordeaux, France). He co-authored more than 30 papers for the last ten years.

Professor J.R. Morante is full professor of the Faculty of Physics of the University of Barcelona. Since 2009 he has been director of the advanced materials area of the Energy Research Institute of Catalonia, IREC, and since 2015 he was appointed as director of this institute. Currently, he is focused on the energy transfer mechanisms occurring at interfaces involving electrons, photons, phonons and chemicals. He is specialized in the development of renewable energy systems based on nano structures and their functionalization for energy storage. He has co-authored more than 600 publications, without proceedings and books, with more than 26.900 citations ($h = 86$) according GS data base.

Thierry Brousse is a Professor of Materials Science at the University of Nantes. He received his PhD degree in 1991. After being a chemical engineer in a company, he joined the University of Nantes in 1994. His research at IMN focuses on innovative materials for electrochemical capacitors and related devices. He is Associate Editor for the Journal of The Electrochemical Society. He has mentored 23 PhD students. With his team as well as international collaborators, he co-authored more than 160 peer-reviewed journal publications and book chapters. He is currently vice-dean of the University of Nantes in charge of Technology Transfer.

Dr. Yury Gogotsi is Charles T. and Ruth M. Bach Chair Professor and Distinguished University Professor of Materials Science and Engineering at Drexel University in Philadelphia, USA. He also serves as Director of the A.J. Drexel Nanomaterials Institute. His research group works on nanostructured carbons, 2D carbides and nitrides, as well as other nanomaterials for energy, water and biomedical applications. He has co-authored 2 books, 16 book chapters, more than 600 journal papers, edited 14 books, and obtained more than 50 patents. He was recognized as Highly Cited Researcher in Materials Science and Chemistry (Web of Science) in 2014–2018. He has received numerous national and international awards for his research. He also serves on the MRS Board of Directors and acts as Associate Editor of ACS Nano